Journal of Quality Measurement and Analysis
e-ISSN: 2600-8602
https://doi.org/10.17576/jqma.2104.2025.06

JQMA 21(4) 2025, 93-115
http://www.ukm.my/jqma

UNSTEADY TWO-PHASE DUSTY FLUID FLOW OVER A CONE IN A POROUS MEDIUM WITH CONSTANT WALL TEMPERATURE

(*Aliran Bendalir Berdebu Dua Fasa Tak Mantap Melintasi Kon dalam Medium Berliang dengan Suhu Dinding Malar*)

HAJAR HANAFI, LIM YEOU JIANN, HANIFA HANIF & SHARIDAN SHAFIE*

ABSTRACT

Dusty fluid flow, which consists of mixtures of solid particles with a carrier fluid, is significant in many natural and engineered systems. This study focuses on unsteady dusty fluid flow over a cone immersed in a porous medium, considering the effects of a magnetic field, heat generation/absorption, and thermal radiation. The combination of dusty fluid and cone geometry reflects real-world multiphase flows over sloped surfaces, typical of geothermal reservoirs. The Crank-Nicolson approach is applied to solve the developed nonlinear governing equations with the subjected initial and boundary conditions. The analysis through graphs and tables examines the impacts of the fluid-particle interaction under the influence of the considered effects on the dusty fluid flow characteristics. The current study's restricted cases were compared to numerical findings and found to be in great agreement. The results indicate that an increase in the fluid-particle interaction parameter enhances the velocity profiles of the particle phase while causing a decline in the fluid phase. For fluid phase, the fluid-particle interaction parameter diminishes the local Nusselt number by 15.8% and the local skin friction by 4.8%. Additionally, the particle phase mass concentration parameter decreases the local Nusselt number by 23% and the local skin friction by 12.3%. This model is relevant for geothermal energy extraction, where multiphase dusty flows occur through porous, inclined rock formations under varying thermal and magnetic conditions.

Keywords: dusty fluid; magnetohydrodynamic; Crank–Nicolson method; cone

ABSTRAK

Aliran bendalir berdebu, yang terdiri daripada campuran zarah pepejal dengan bendalir pembawa, adalah penting dalam banyak sistem semula jadi dan kejuruteraan. Kajian ini menumpukan pada aliran bendalir berdebu yang tak mantap melintasi kon yang terendam dalam medium berliang, dengan mengambil kira kesan medan magnet, penjanaan/penyerapan haba, dan sinaran terma. Gabungan bendalir berdebu dan geometri kon mencerminkan aliran berbilang fasa sebenar di atas permukaan condong, yang biasa ditemui di takungan geoterma. Kaedah Crank-Nicolson digunakan untuk menyelesaikan persamaan kawalan tak linear yang dibangunkan dengan syarat awal dan sempadan yang ditentukan. Analisis melalui graf dan jadual mengkaji kesan interaksi bendalir-zarah di bawah pengaruh faktor-faktor yang dipertimbangkan terhadap ciri-ciri aliran bendalir berdebu. Kes-kes terhad kajian semasa dibandingkan dengan hasil berangka dan menunjukkan persetujuan yang sangat baik. Hasil kajian menunjukkan bahawa peningkatan parameter interaksi bendalir-zarah meningkatkan profil halaju fasa zarah sambil menyebabkan penurunan dalam fasa bendalir. Untuk fasa bendalir, parameter interaksi bendalir-zarah mengurangkan nombor Nusselt tempatan sebanyak 15.8% dan geseran kulit tempatan sebanyak 4.8%. Selain itu, parameter kepekatan jisim fasa zarah mengurangkan nombor Nusselt tempatan sebanyak 23% dan geseran kulit tempatan sebanyak 12.3%. Model ini berkaitan dengan pengekstrakan tenaga geoterma, di mana aliran berbilang fasa berdebu berlaku melalui formasi batuan berliang dan condong di bawah keadaan terma dan magnetik yang berubah-ubah.

Kata kunci: bendalir berdebu; magnetohidrodinamik; kaedah Crank–Nicolson; kon

1. Introduction

Dusty fluid can be found in many engineering applications such as automotive, chemical, coating, and environmental industries. Dusty fluid flow has been used to illuminate multiphase flow phenomena and the dynamic behaviour of mixtures containing solid particles and liquid or gas phases. Many scientists are interested in the phenomena of airflow carrying microscopic dust particles due to its far-reaching implications across environmental science, agriculture, public health, climate research and various scientific disciplines (Sproull 1961). Saffman (1962) investigated how dust particles affected a gas's stability of flow, which is defined by two factors, dust concentration and relaxation time. Then, Kliegel and Nickerson (1962) found agreement between the theoretical predictions and the experimental data for the study of dusty fluid. Most fluid-related difficulties involving two phases are linear and designed for steady-state conditions. Rafiq *et al.* (2021) examined how non-linear thermal radiation affected the flow of suspended solids in the boundary layer of the rotating axisymmetric hemisphere. It was noted that surface heating and thermal radiation can affect the contaminated suspension's heat transport phenomenon. This should be considered if significant heat transfer is anticipated in the flow field. Recently, Mahabaleshwar *et al.* (2023) presented an analytical approach that incorporates mass flow into the boundary layer flow from a two-phase dusty fluid flow model. The strength of the particle interaction parameter was observed to grow as the thickness of the solution domain increased. Rahman *et al.* (2024) explored steady dust particles fluid flow across a stretched sheet using porous dissipation and frictional heating. It was noted that the temperature profile rises for both the fluid and dusty phases with an increase in Brinkman number. The study conducted by Khan *et al.* (2023) examined the accurate solutions and contrasted the impact of fluid and dust particles in the context of Brinkman fluid flow between vertical parallel plates. The distribution of fluid velocities and dust particles was shown to be diminished by the magnetic field and dusty fluid parameter on the fluid flow.

The majority of the above listed studies only examined steady-state scenarios and ignored temporal impacts. By including time into mathematical models, transport phenomena can be better understood and changes in flow characteristics can be addressed with greater accuracy. Understanding unstable flow is vital because flow conditions commonly change over time. The unsteady flow of a dusty fluid has various applications, including particle sorting, sedimentation, and underground disposal of radioactive waste materials. That being said, not much research has been done on the time-dependent unsteady flow, despite its importance to contemporary industry. Sandeep *et al.* (2016) demonstrated and discussed MHD radiative flow over an exponentially permeable stretching surface. It was noted that increasing the fluid-particle interaction parameter leads to faster heat transfer and lower friction. In addition, the stretching/shrinking flow of a fluid-particle suspension in the presence of a continuous suction and dust particle slip on the surface was studied numerically by Hamid *et al.* (2018). It was found that the particle loading parameter and the fluid-particle interaction parameter were the main parameters that influenced the fluid-phase flow. Furthermore, Attia and Ewis (2019) examined the MHD flow of continuous dusty particles and non-Newtonian Darcy fluids between parallel plates. It was discovered that the particle phase takes longer to attain its steady state than the fluid phase.

The study of dusty fluid flow around a cone is a complex and significant area of research with applications in various fields. Understanding the behavior of dusty fluids in unsteady flow conditions around a cone is crucial for practical applications and theoretical advancements. It serves as a representative model for complex flow patterns providing practical applications in technology field which manufactures reliable equipments and different kinds of aircraft propulsion devices, missiles, space vehicles and satellites (Sambath 2017). Siddiqa *et al.* (2017, 2018a) investigate the comprehensive steady flow formations of gas and particle phases along a cone, aiming to predict the behavior of heat transport across the heated cone. The former study emphasizes temperature-dependent properties and general flow behavior, while the latter study investigates the impact of surface irregularities on heat transfer and fluid dynamics. It was discovered that when the mass concentration parameter is increased, skin friction lowers because

the carrier fluid's velocity is reduced relative to the pure fluid case as a result of the fluid losing kinetic and thermal energy through interaction with the dust particles. The impact of non-linear surface radiation on the flow of steady Casson dusty particle suspension across a vertically wavy cone was examined by Siddiqa *et al.* (2018b). The rate of heat transmission was observed to decrease when the surface radiation parameter increased. Palani and Lalith Kumar (2021) studied the movement of gas containing dust particles over a semi-infinite vertical cone. Dust particles in the liquid were discovered to cause the velocity of the dusty gas to decrease relative to the velocity of the dust-free gas because the dusty particles impede the flow of the gas. Besides, Nabwey and Mahdy (2021) has conducted research on micropolar dusty fluid flow in a vertical permeable cone. It was noted that increased values of the particle phase mass concentration parameter result in decreased both fluid and particle velocity profiles. There are several interesting studies on the heat transfer rates of dusty fluids in various geometries can be found in Jagannadham *et al.* (2022), Bibi *et al.* (2022), Fathy and Sayed (2022) and Reddimalla *et al.* (2022) which focus on geometries such as a horizontal flat plate, a tangent hyperbolic surface, a stretching surface, and a circular pipe, respectively.

Porous media, such as soil and rocks, are vital in groundwater flow, environmental protection, oil recovery, heat transfer, and more. Understanding them is essential for managing water resources, remediating contamination, and optimizing various industrial processes (Bear 2013). Porous materials contribute to advancements in technology, environmental sustainability, and resource management across diverse fields. The investigation of fluid flow in porous media has captured the interest of a significant number of researchers because of the possible uses. It has been established that the medium porosity and permeability had an impact on the flow rate of the fluid (Ahmad *et al.* 2019). Porous media and dusty fluid flow study together provide a holistic understanding of complex systems where fluid interacts with solid particles. Attia *et al.* (2012) investigated the influence of porosity and particle-phase viscosity on the velocity of the fluid and particle-phases in circular pipe. It was found that lesser velocity gradients near the wall are the result of the particle suspension in the pipe moving less when the magnetic field becomes stronger. This directly lowers both phases' skin-friction coefficients. Saxena and Agarwal (2014) highlighted the unsteady flow of a dusty fluid between two parallel plates when the upper plate is restricted by a porous medium. According to the findings, the fluid and particle velocity distribution increases in the porous medium halfway through and then declines. Anand *et al.* (2015) focused on the analysis of the MHD flow of a dusty fluid through a porous material between parallel plates. When the magnetic field is increased, it is noticed that the velocity increases in the upper plate and decreases in the bottom plate. Besides, research has been done by Madhura and Uma (2016) on the uniform distribution of dust particles in a restricted channel containing an unstable incompressible electrically conducting fluid flow. The fluid particles were found to reach the steady state sooner than the dust particles. This discrepancy results from the fluid being directly subjected to the time-dependent pressure gradient. From the plots, it was clear that the fluid flow is parallel to the particle flow. Vidhya *et al.* (2017) investigated the impact of a viscous incompressible dusty fluid passing through a densely porous media confined by a vertical infinite plane surface. When the particle phase mass concentration parameter increases, it was found that there are greater differences in the velocities between the dust particles and the dusty fluid. In addition, hydromagnetic oscillatory flow and heat transfer in dusty viscoelastic fluid via a porous material in an inclined channel have been investigated in Chand (2018) . Dust particle velocity profiles behave similarly to fluid velocity profiles, with fluid phase velocity being greater than particle phase velocity.

While unsteady dusty fluid flow has been studied in a variety of geometries, including parallel plates and channels, limited attention has been given to unsteady flow over a vertical cone in the presence of additional physical effects. Most existing works on conical geometries have primarily focused on steady-state analyses. The present study addresses this gap by extending the work of Siddiqa *et al.* (2017) and Palani and Laltih Kumar (2021) to consider unsteady MHD radiative dusty fluid flow over a vertical cone embedded in a porous medium, with additional effects of heat generation/absorption and a constant wall temperature. This study contributes a

novel numerical investigation that incorporates these complex effects into the governing equations. The resulting nonlinear, coupled partial differential equations are solved using the Crank-Nicolson method and Thomas algorithm (Hanif *et al.* 2020; Blottner 1970), and quantitative results are obtained and visualized using MATLAB.

2. Mathematical Formulation

The current study investigates the unsteady dusty fluid flow across a vertical cone with a radius described by the function $r(r = x \sin \alpha)$ in the presence of a magnetic field, thermal radiation and heat generation/absorption. The horizontal $y-$axis corresponds to the cone's surface, whilst the vertical $x-$-axis corresponds to the cone's normal. The temperature distribution on the cone's surface is assumed to be the same as that of the surrounding fluid, denoted as T_∞, when t is less than zero. Following this, once the fluid's temperature exceeds zero, the surface of the cone rises to a designated value represented as T_w and remained constant after that. The solid particles are supposed to be spherical in shape, constant in size and non-reacting. Additionally, it is assumed that the density of dust particles are consistent throughout the flow. Moreover, the fluid and the dust particles are initially assumed to be static (Isa *et al.* 2016). The external electric field is considered to be zero and the potential influence of polarization-induced external electrical fields are negligible (Manjunatha *et al.* 2013). It is assumed that the magnetic field is homogeneous and parallel to the y-axis, as depicted in Figure 1. Considering the previously mentioned assumptions, the governing equations for fluid and particle phases can be formulated as follows (Sambath 2017),

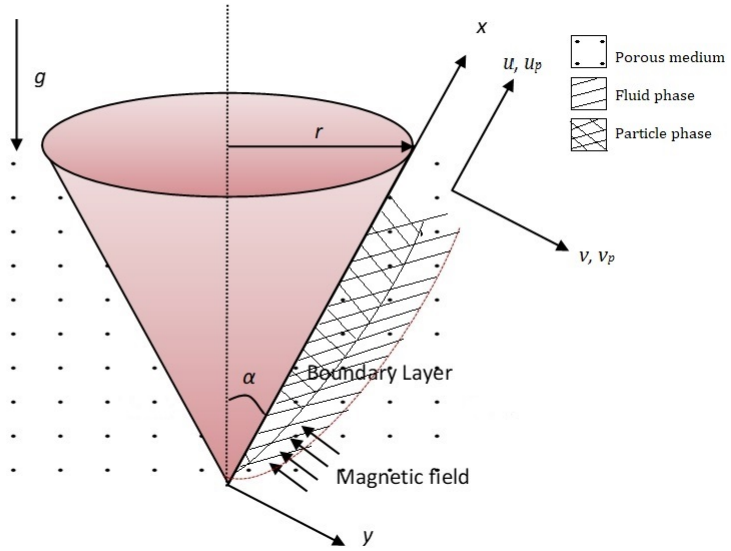

Figure 1: Geometric coordinates system and problem layouts

Continuity equation:

$$\boldsymbol{\nabla}.\big(r\mathbf{V}\big) = 0, \tag{1}$$

$$\boldsymbol{\nabla}.\big(r\mathbf{V}_p\big) = 0, \tag{2}$$

Momentum equation:

$$\rho\left(\frac{\partial u}{\partial t}+(\mathbf{V}.\boldsymbol{\nabla})u\right)=\mu\frac{\partial^2 u}{\partial y^2}+g(\rho\beta_T)\cos\alpha(T-T_\infty)-\sigma B^2u-\frac{\mu}{k_0}u+\frac{\rho_p}{\tau_m}(u_p-u), \quad (3)$$

$$\rho_p\left(\frac{\partial u_p}{\partial t}+(\mathbf{V}_p.\boldsymbol{\nabla})u_p\right)=-\frac{\rho_p}{\tau_m}(u_p-u), \quad (4)$$

Energy equation:

$$\rho C_p\left(\frac{\partial T}{\partial T}+(\mathbf{V}.\boldsymbol{\nabla})T\right)=k\frac{\partial^2 T}{\partial y^2}-\frac{\partial q_r}{\partial y}+Q_0(T-T_\infty)+\frac{\rho_p C_s}{\tau_T}(T_p-T), \quad (5)$$

$$\rho_p C_s\left(\frac{\partial T_p}{\partial t}+(\mathbf{V}_p.\boldsymbol{\nabla})T_p\right)=-\frac{\rho_p C_s}{\tau_T}(T_p-T), \quad (6)$$

The Rosseland approximation for the radiative heat flux q_r is (Magyari & Pantokratoras 2011),

$$q_r=-\frac{4\sigma_s}{3k_e}\frac{\partial T_\infty^4}{\partial y}. \quad (7)$$

The temperature changes in the flow are thought to be negligibly small, allowing T_∞^4 to be described as a temperature linear function. This is done by removing higher-order terms and expanding T_∞^4 around T_∞ in the Taylor series. Eventually,

$$T^4\cong 4T_\infty^3T-3T_\infty^4. \quad (8)$$

By using Eq. 7 and 8, Eq. 5 may be expressed as follows,

$$\rho C_p\left(\frac{\partial T}{\partial t}+(\mathbf{V}.\boldsymbol{\nabla})T\right)=k\frac{\partial^2 T}{\partial y^2}+\frac{16\sigma_s T_\infty^3}{3k_e}\frac{\partial^2 T}{\partial y^2}+Q_0(T-T_\infty)+\frac{\rho_p C_s}{\tau_T}(T_p-T). \quad (9)$$

The initial and boundary conditions are (Chamkha *et al.* 2012),

$$\begin{aligned}
&t\le 0:(u,u_p)=0,(v,v_p)=0,(T,T_p)=T_\infty \text{ for all } x \text{ and } y,\\
&t>0:(u,u_p)=0,(v,v_p)=0,(T,T_p)=T_w \text{ at } y=0,\\
&(u,u_p)=0,(T,T_p)=T_\infty \text{ at } x=0,\\
&(u,u_p)\to 0,(T,T_p)\to T_\infty \text{ as } y\to\infty.
\end{aligned} \quad (10)$$

The subsequent physical quantities represent the local shear stress and local Nusselt number for fluid phase, respectively (Hasan & Mujumdar 1984).

$$\tau_x=\mu\left(\frac{\partial u}{\partial y}\right)_{y=0}, \quad (11)$$

$$Nu_x = \frac{-x\left(\frac{\partial T}{\partial y}\right)_{y=0}}{T_w - T_\infty}. \tag{12}$$

Using dimensionless parameter (Sivaraj & Kumar 2013),

$$\begin{aligned} &\xi = \frac{x}{L}, \eta = \frac{y}{L}(Gr_L)^{\frac{1}{4}}, R^* = \frac{r}{L}, \big(v, v_p\big)^* = \frac{L}{\nu}\big(Gr_L\big)^{-\frac{1}{4}}(v, v_p), \\ &\big(u, u_p\big)^* = \frac{L}{\nu}\big(Gr_L\big)^{-\frac{1}{2}}(u, u_p), t^* = \frac{\nu t}{L^2}\big(Gr_L\big)^{\frac{1}{2}}, \big(T, T_p\big)^* = \frac{\big(T, T_p\big) - T_\infty}{T_w - T_\infty}. \end{aligned} \tag{13}$$

Eq. 1 to 6 are then reduced to the following dimensionless form, (for convenience, remove * sign)

$$\frac{\partial u}{\partial \xi} + \frac{\partial v}{\partial \eta} + \frac{u}{\xi} = 0, \tag{14}$$

$$\frac{\partial u_p}{\partial \xi} + \frac{\partial v_p}{\partial \eta} + \frac{u_p}{\xi} = 0, \tag{15}$$

$$\frac{\partial u}{\partial t} + u\frac{\partial u}{\partial \xi} + v\frac{\partial u}{\partial \eta} = \frac{\partial^2 u}{\partial \eta^2} + T\cos\alpha - \left(M + \frac{1}{K}\right)u + D_p\alpha_d\big(u_p - u\big), \tag{16}$$

$$\frac{\partial u_p}{\partial t} + u_p\frac{\partial u_p}{\partial \xi} + v_p\frac{\partial u_p}{\partial \eta} = -\alpha_d\big(u_p - u\big), \tag{17}$$

$$\frac{\partial T}{\partial t} + u\frac{\partial T}{\partial \xi} + v\frac{\partial T}{\partial \eta} = \left(\frac{1 + Rd}{Pr}\right)\frac{\partial^2 T}{\partial \eta^2} + QT + \frac{2}{3Pr}D_p\alpha_d\big(T_p - T\big), \tag{18}$$

$$\frac{\partial T_p}{\partial t} + u_p\frac{\partial T_p}{\partial \xi} + v_p\frac{\partial T_p}{\partial \eta} = -\frac{2}{3\gamma Pr}\alpha_d\big(T_p - T\big), \tag{19}$$

where,

$$\begin{aligned} &Pr = \frac{\nu_f}{\alpha}, \gamma = \frac{C_s}{C_p}, \tau_T = \frac{3}{2}\gamma\tau_m Pr, D_p = \frac{\rho_p}{\rho}, \alpha_d = \frac{L^2}{v_f\tau_m}\big(Gr_L\big)^{-\frac{1}{2}}, \\ &M = \frac{\sigma B^2 L^2}{\mu}\big(Gr_L\big)^{-\frac{1}{2}}, \frac{1}{K} = \frac{L^2}{k_0}\big(Gr_L\big)^{-\frac{1}{2}}, Rd = \frac{16\sigma_s T_\infty^{*^3}}{3k_e k}, Q = \frac{Q_0 L^2}{\mu C_p}\big(Gr_L\big)^{-\frac{1}{2}}. \end{aligned} \tag{20}$$

The dimensionless initial and boundary conditions are as follows,

$$\begin{aligned}
&t \le 0 : \big(u, u_p\big) = 0, \big(v, v_p\big) = 0, \big(T, T_p\big) = 0 \text{ for all } \xi \text{ and } \eta,\\
&t > 0 : \big(u, u_p\big) = 0, \big(v, v_p\big) = 0, \big(T, T_p\big) = 1 \text{ at } \eta = 0,\\
&\big(u, u_p\big) = 0, \big(T, T_p\big) = 0 \text{ at } \xi = 0,\\
&\big(u, u_p\big) \to 0, \big(T, T_p\big) \to 0 \text{ as } \eta \to \infty.
\end{aligned} \tag{21}$$

The dimensionless local shear stress and local Nusselt number for fluid phase are provided by,

$$\tau_\xi = {Gr_L}^{\frac{3}{4}} \left(\frac{\partial u}{\partial \eta} \right)_{\eta=0}, \tag{22}$$

$$Nu_\xi = {Gr_L}^{\frac{1}{4}} \frac{\xi}{T_{\eta=0}} \left(- \frac{\partial T}{\partial \eta} \right)_{\eta=0}. \tag{23}$$

2.1. *Numerical Procedure of Crank–Nicolson*

The Crank Nicolson discretization method is used to solve the governing equation Eq. 14 to 19. This implicit finite difference scheme exhibits rapid convergence, precision, and dependability in addition to being unconditionally stable (Luskin *et al.* 1982). It approximates a derivative term at the average of current and forward time level. Let $u_{i,j}^k$, $v_{i,j}^k$ and $T_{i,j}^k$ be the numerical approximations of $u(\xi, \eta, t), v(\xi, \eta, t)$ and $T(\xi, \eta, t)$ at time k for any point in coupled Eq. 14 to 19, the subsequent equations are considered (Sun & Trueman 2006),

$$\begin{aligned}
&\frac{u_{i,j}^{k+1} - u_{i-1,j}^{k+1} + u_{i,j}^k - u_{i-1,j}^k}{2\Delta\xi} + \frac{v_{i,j}^{k+1} - v_{i,j-1}^{k+1} + v_{i,j}^k - v_{i,j-1}^k}{2\Delta\eta}\\
&+ \frac{1}{\xi_i} \frac{u_{i,j}^{k+1} + u_{i,j}^k}{2} = 0,
\end{aligned} \tag{24}$$

$$\begin{aligned}
&\frac{u_{p_{i,j}}^{k+1} - u_{p_{i-1,j}}^{k+1} + u_{p_{i,j}}^k - u_{p_{i-1,j}}^k}{2\Delta\xi} + \frac{v_{p_{i,j}}^{k+1} - v_{p_{i,j-1}}^{k+1} + v_{p_{i,j}}^k - v_{p_{i,j-1}}^k}{2\Delta\eta}\\
&+ \frac{1}{\xi_i} \frac{u_{p_{i,j}}^{k+1} + u_{p_{i,j}}^k}{2} = 0,
\end{aligned} \tag{25}$$

$$\begin{aligned}
&\left(\frac{u_{i,j}^{k+1} - u_{i,j}^k}{\Delta t} \right) + u_{i,j}^k \left(\frac{u_{i,j}^{k+1} - u_{i-1,j}^{k+1} + u_{i,j}^k - u_{i-1,j}^k}{2\Delta\xi} \right)\\
&+ v_{i,j}^k \left(\frac{u_{i,j+1}^{k+1} - u_{i,j-1}^{k+1} + u_{i,j+1}^k - u_{i,j-1}^k}{4\Delta\eta} \right)\\
&= \frac{u_{i,j+1}^{k+1} - 2u_{i,j}^{k+1} + u_{i,j-1}^{k+1} + u_{i,j+1}^k - 2u_{i,j}^k + u_{i,j-1}^k}{2\big(\Delta\eta\big)^2} + \frac{T_{i,j}^{k+1} + T_{i,j}^k}{2} \cos\alpha
\end{aligned}$$

$$-\left(M+\frac{1}{K}\right)\frac{u_{i,j}^{k+1}+u_{i,j}^{k}}{2}+D_p\alpha_d\left(\frac{u_{p_{i,j}}^{k+1}+u_{p_{i,j}}^{k}}{2}-\frac{u_{i,j}^{k+1}+u_{i,j}^{k}}{2}\right), \tag{26}$$

$$\begin{aligned}&\left(\frac{u_{p_{i,j}}^{k+1}-u_{p_{i,j}}^{k}}{\Delta t}\right)+u_{p_{i,j}}^{k}\left(\frac{u_{p_{i,j}}^{k+1}-u_{p_{i-1,j}}^{k+1}+u_{p_{i,j}}^{k}-u_{p_{i-1,j}}^{k}}{2\Delta\xi}\right)\\&+v_{p_{i,j}}^{k}\left(\frac{u_{p_{i,j+1}}^{k+1}-u_{p_{i,j-1}}^{k+1}+u_{p_{i,j+1}}^{k}-u_{p_{i,j-1}}^{k}}{4\Delta\eta}\right)\\&=-\alpha_d\left(\frac{u_{p_{i,j}}^{k+1}+u_{p_{i,j}}^{k}}{2}-\frac{u_{i,j}^{k+1}+u_{i,j}^{k}}{2}\right),\end{aligned} \tag{27}$$

$$\begin{aligned}&\left(\frac{T_{i,j}^{k+1}-T_{i,j}^{k}}{\Delta t}\right)+u_{i,j}^{k}\left(\frac{T_{i,j}^{k+1}-T_{i-1,j}^{k+1}+T_{i,j}^{k}-T_{i-1,j}^{k}}{2\Delta\xi}\right)\\&+v_{i,j}^{k}\left(\frac{T_{i,j+1}^{k+1}-T_{i,j-1}^{k+1}+T_{i,j+1}^{k}-T_{i,j-1}^{k}}{4\Delta\eta}\right)\\&=\left(\frac{1+Rd}{Pr}\right)\left(\frac{T_{i,j+1}^{k+1}-2T_{i,j}^{k+1}+T_{i,j-1}^{k+1}+T_{i,j+1}^{k}-2T_{i,j}^{k}+T_{i,j-1}^{k}}{2\left(\Delta\eta\right)^2}\right)\\&+Q\frac{T_{i,j}^{k+1}+T_{i,j}^{k}}{2}+\frac{2}{3Pr}D_p\alpha_d\left(\frac{T_{p_{i,j}}^{k+1}+T_{p_{i,j}}^{k}}{2}-\frac{T_{i,j}^{k+1}+T_{i,j}^{k}}{2}\right),\end{aligned} \tag{28}$$

$$\begin{aligned}&\left(\frac{T_{p_{i,j}}^{k+1}-T_{p_{i,j}}^{k}}{\Delta t}\right)+u_{p_{i,j}}^{k}\left(\frac{T_{p_{i,j}}^{k+1}-T_{p_{i-1,j}}^{k+1}+T_{p_{i,j}}^{k}-T_{p_{i-1,j}}^{k}}{2\Delta\xi}\right)\\&+v_{p_{i,j}}^{k}\left(\frac{T_{p_{i,j+1}}^{k+1}-T_{p_{i,j-1}}^{k+1}+T_{p_{i,j+1}}^{k}-T_{p_{i,j-1}}^{k}}{4\Delta\eta}\right)\\&=-\frac{2}{3\gamma Pr}\alpha_d\left(\frac{T_{p_{i,j}}^{k+1}+T_{p_{i,j}}^{k}}{2}-\frac{T_{i,j}^{k+1}+T_{i,j}^{k}}{2}\right).\end{aligned} \tag{29}$$

Here's a brief overview of how it works:

(1) The method starts by discretizing the spatial and temporal domains of the PDE into a grid as shown in Figure 2.
(2) The derivatives in the PDE are approximated using finite difference methods. In the Crank-Nicolson method, a central difference approximation is often used for both time and space derivatives. See: Eq. 24 to 29
(3) The resulting discretized system of equations is usually a system of linear equations and resulting in the conversion to a tridiagonal system. The Crank-Nicolson method then solves this system to obtain the solution at the next time step.
(4) The process is typically iterated until the solution converges to a desired level of accuracy.

The Crank-Nicolson method is often favored because it is numerically stable and converges quickly for a wide range of problems. It is particularly useful for problems where stability is a

concern, such as when dealing with stiff equations.

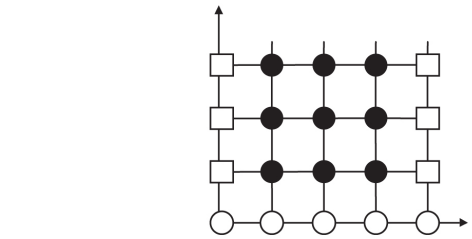

□ The points calculated using boundary conditions.
● The grid points approximated using finite difference method.
○ The points calculated using initial condition.

Figure 2: Crank-Nicolson method mesh diagram

The rectangular domain is considered when $(\xi_{max}, \eta_{max}) = (1, 20)$, where η_{max} is regarded as $\eta \to \infty$ and well outside the boundary layers. This action is taken in order to satisfy the boundary conditions outlined in Eq. 21. The mesh spacing in the ξ and η directions, $\Delta\xi = 0.05$, $\Delta\eta = 0.05$, and $\Delta t = 0.01$ is selected to obtain the tolerance limit within 10^{-5}. The process of performing calculations is iterated until a steady state is achieved. A convergence criterion is employed that relies on the relative difference between the values of two consecutive iterations. The iterative procedure is completed when the solution satisfies the convergence criterion, which is defined as the point when the difference becomes smaller than 10^{-5} at all grid points. The scheme exhibits unconditional stability. The local truncation error is $O(\Delta t^2 + \Delta\xi^2 + \Delta\eta^2)$ and converges to zero as Δt, $\Delta\xi$ and $\Delta\eta$ approach zero. It can be inferred that the Crank-Nicolson approach is compatible. The convergence is ensured via stability and compatibility (Adak 2018).

3. Results and Discussions

Table 1 depicts the validation of the obtained results by comparing with Hering and Grosh (1962) and Sambath (2017) in the limiting case without considering the particle phase. The solutions shows good agreement. This has improved the confidence and the accuracy of the proposed method and the present determined results. Based on Pullepu *et al.* (2007, 2012) and Thandapani *et al.* (2012), the default parametric values $t = 10$, α= 20°, $Pr = 7.0$, $Rd = 1$, $M = K = 2$, $Q = \alpha_d = 0.5$, $D_p = 10$ and $\gamma = 0.1$ are fixed, unless explicitly stated in the corresponding graph.

Table 1: Comparison of $Nu_\xi/{Gr_L}^{\frac{1}{4}}$ at $Rd = M = \frac{1}{K} = Q = \alpha_d = D_p = 0$ and $\gamma = 1$ at $\xi = 1$

Pr	Hering & Grosh (1962) $-\theta'(0) * \sqrt{\mathrm{Pr}}$	Sambath (2017) $Nu_x/{Gr_L}^{\frac{1}{4}}$	Present Results $Nu_x/{Gr_L}^{\frac{1}{4}}$
0.03	0.1244	0.1243	0.1247
0.1	0.2113	0.2115	0.2124
0.7	0.4511	0.4529	0.4591
1.0	0.5104	0.5125	0.5211

Figure 3 indicates the unsteady distributions of u and u_p at several numerical quantities of Pr. The increase in the value of the parameter Pr leads to a decrease in the variables u and u_p.

A decrease in thermal diffusivity and velocity occurs as Pr increases because of the adhesive properties of the fluid, which causes the force to grow. The heavier the momentum barrier layer becomes heavier, leading to a thicker shape. Moreover, the values needed to reach a steady state grow with rising Pr. Figure 4 reveals the unsteady distributions of T and T_p at several

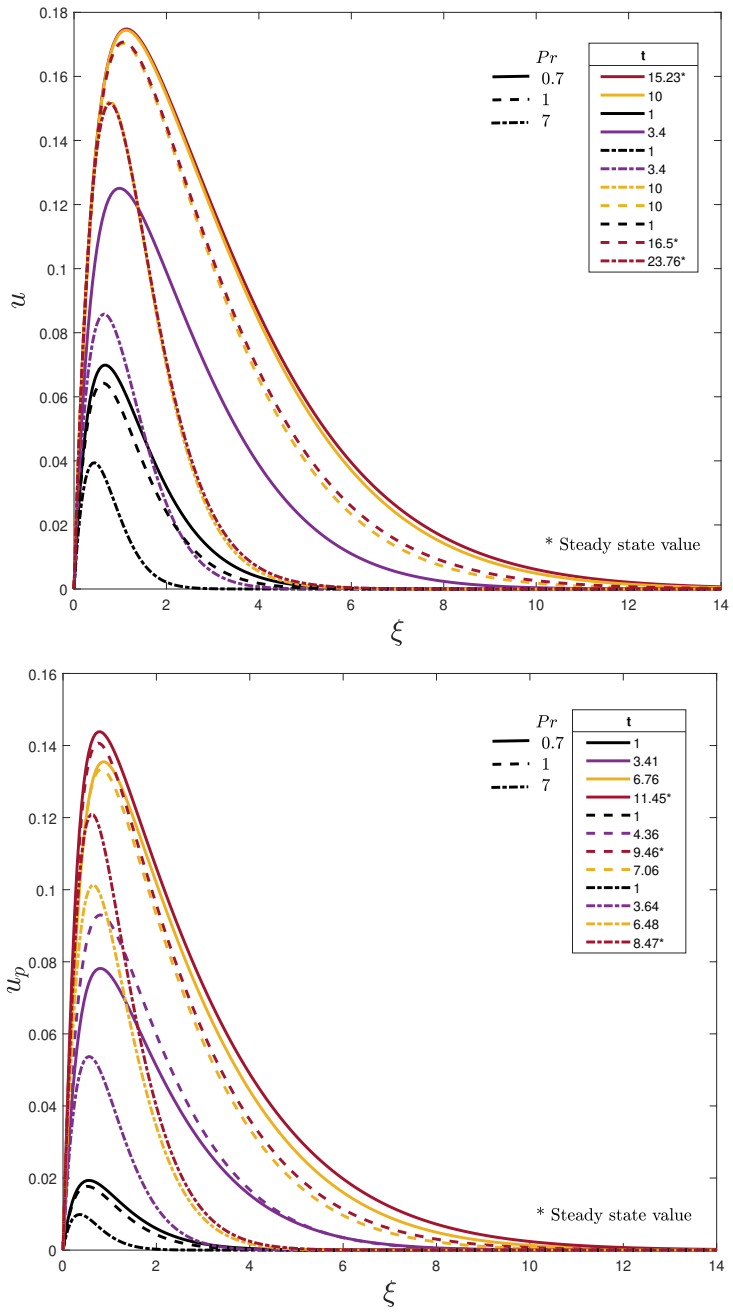

Figure 3: Unsteady distributions of velocity at several numerical quantities of Prandtl number, Pr

numerical quantities of Pr. The findings show that higher reveal that higher values of Pr lead to steeper temperature gradients and thinner thermal boundary layers compared to lower Pr. This is due to the increasing viscosity of the liquid. It further appears that as Pr increases, the values needed to reach a steady state decrease. This is because, as Pr increases, momentum

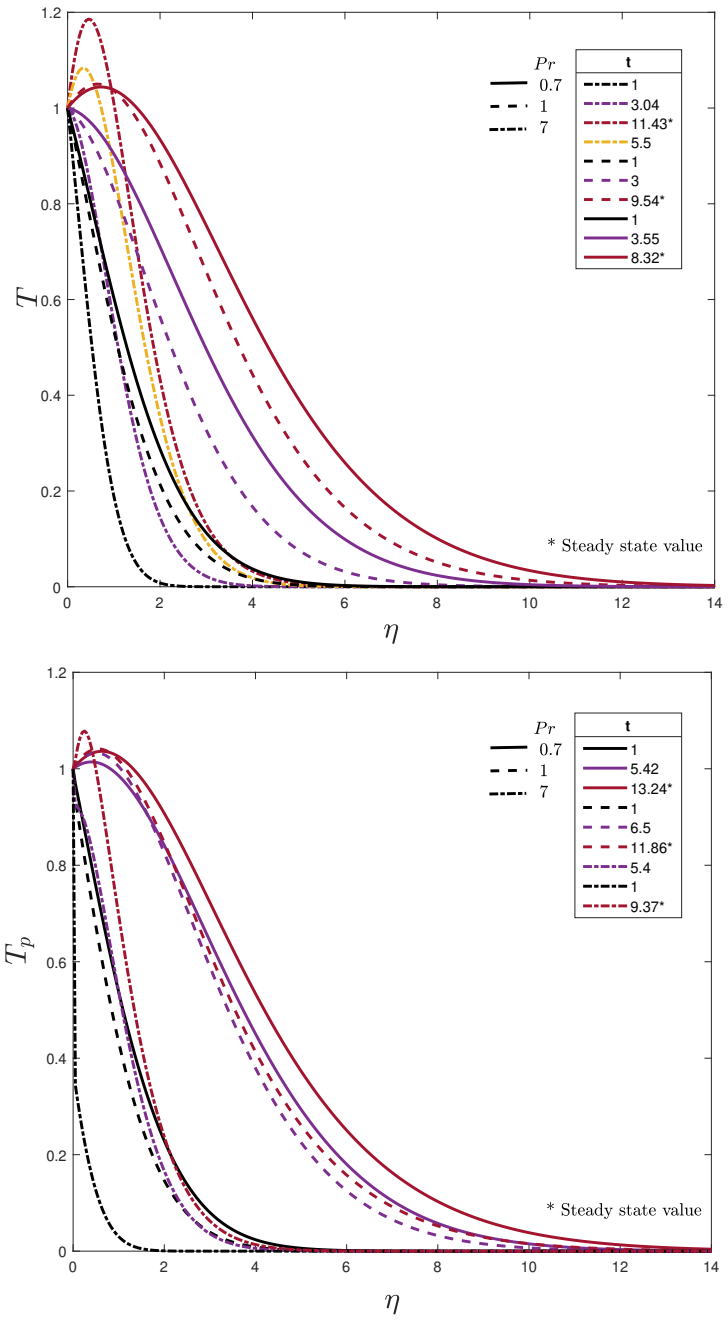

Figure 4: Unsteady distributions of temperature at several numerical quantities of Prandtl number, Pr

diffusion dominates over thermal diffusion, causing the velocity profile to stabilize faster, which in turn reduces the time or values needed to reach a steady state in the system. This behavior is consistent with the findings of Kays and Crawford (1980), who established that fluids with higher Pr have lower thermal diffusivity, resulting in enhanced heat transfer near the cone's surface. Similarly, Immanuel *et al.* (2019) observed a similar trend for natural convection flow past a vertical cone, reinforcing the correlation between Pr and the rate of heat transfer. The parameter t is crucial for understanding the transient behavior of unsteady flows, as shown in Figures 3 and 4. The chosen values of t highlight the evolution of velocity and thermal profiles

over time, illustrating the transition from initial conditions to steady-state. By plotting t for different Pr, it demonstrates how fluids with varying thermal diffusivities respond temporally. The results align with Mohiddin *et al.* (2012), who demonstrated that time-dependent variations in boundary layers are significantly influenced by thermal diffusivity, as captured by Pr.

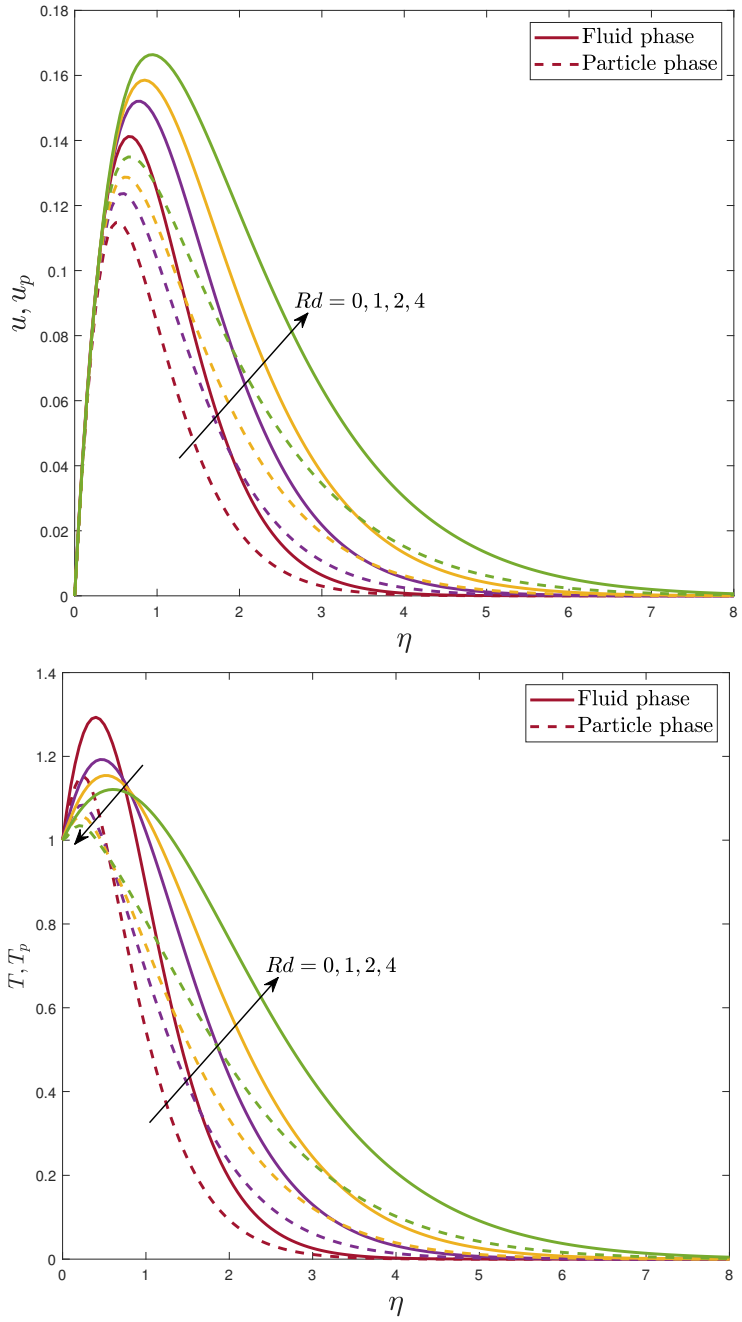

Figure 5: Impacts of thermal radiation, Rd on velocity and temperature distribution

Figure 5 illustrates the impact of Rd on the velocity and temperature distributions. When the value of Rd is increased, there is a rise in both velocities. When Rd rises, there is a corresponding increase in the thermal state of the fluid and the thickness of its thermal boundary layer. The buoyancy effect induces a greater flow within the boundary layer, resulting in an augmentation

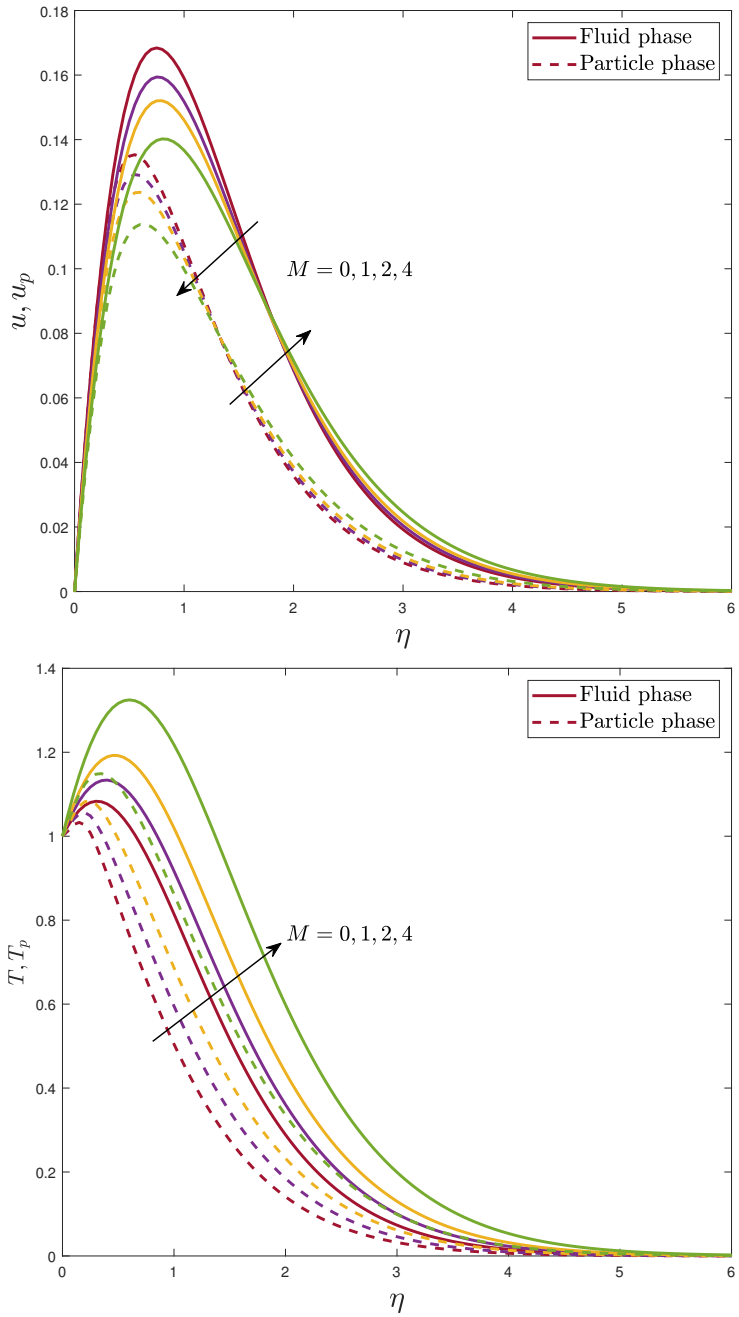

Figure 6: Impacts of magnetic field, M on velocity and temperature distribution

of velocity. Moreover, this graph indicates that for rising Rd, both temperatures are declining at $T : \eta \leq 0.85$ and $T_p : \eta \leq 0.55$, while enhancing at $T : \eta > 0.85$ and $T_p : \eta > 0.55$ (Sandeep *et al.* 2016). To achieve higher values of Rd, the temperature exhibits a reduction in proximity to the surface of the cone while simultaneously increasing as the distance η from the surface increases. As the fluid is displaced from the cone's surface, Rd becomes increasingly evident. Figure 6 displays the impact of M on fluid and particle velocity and temperature distributions. This graph indicates that for rising M, both velocities are declining at $u : \eta \leq 1.8$ and $u_p : \eta \leq 1.3$, while enhancing at $u : \eta > 1.8$ and $u_p : \eta > 1.3$. The figure

shows that as M climbs, so does the temperature. Initially, at lower u and u_p, the magnetic field may not fully saturate or exhibit a strong effect. As the velocities increase, M becomes more saturated, leading to a decrease in the initial M. Moreover, a higher M value inherently promotes temperature dispersion. High M values usually restrict fluid flow. As a result, the thermal boundary layer increases.

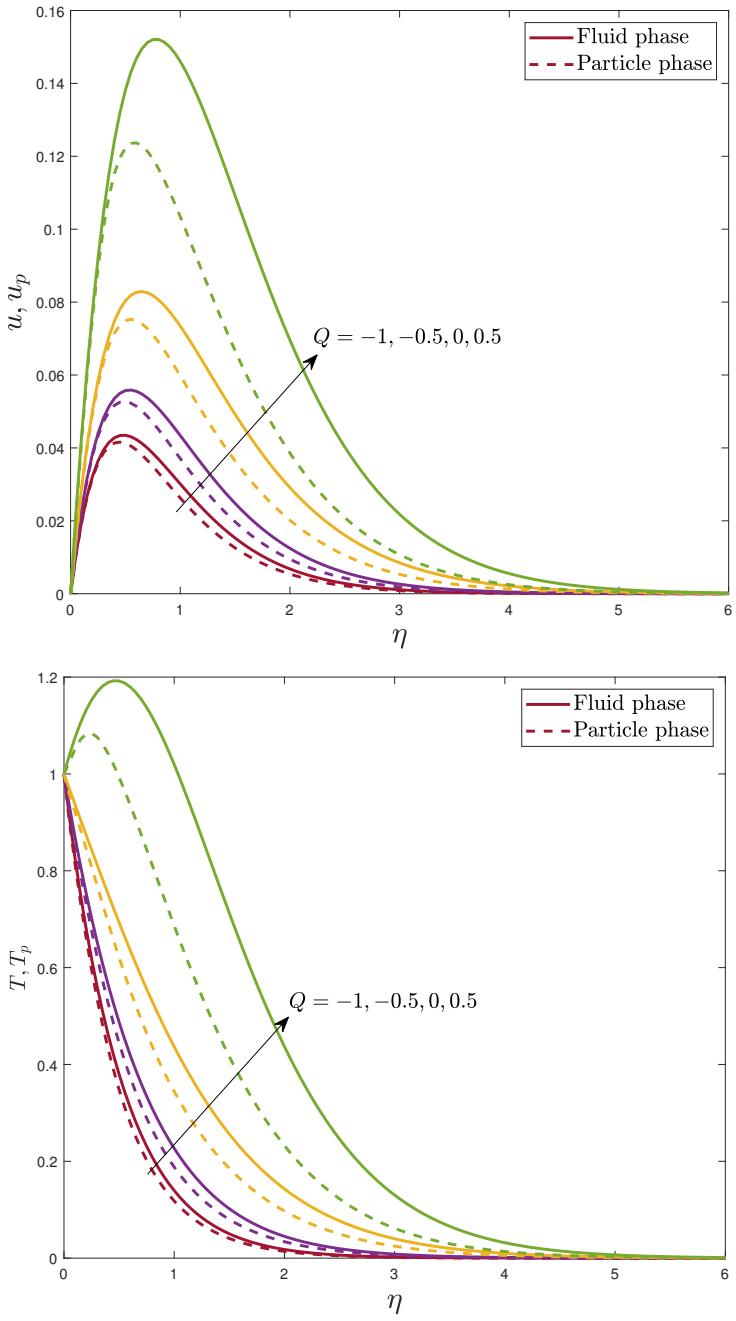

Figure 7: Impacts of heat generation/absorption, Q on velocity and temperature distribution

Figure 7 shows how Q affects fluid and particle velocity and temperature distributions. Both velocities rose with increasing Q. Positive Q indicates heat generation, while negative Q indicates heat absorption. Heat generation increases buoyant forces, which boost fluid flow and

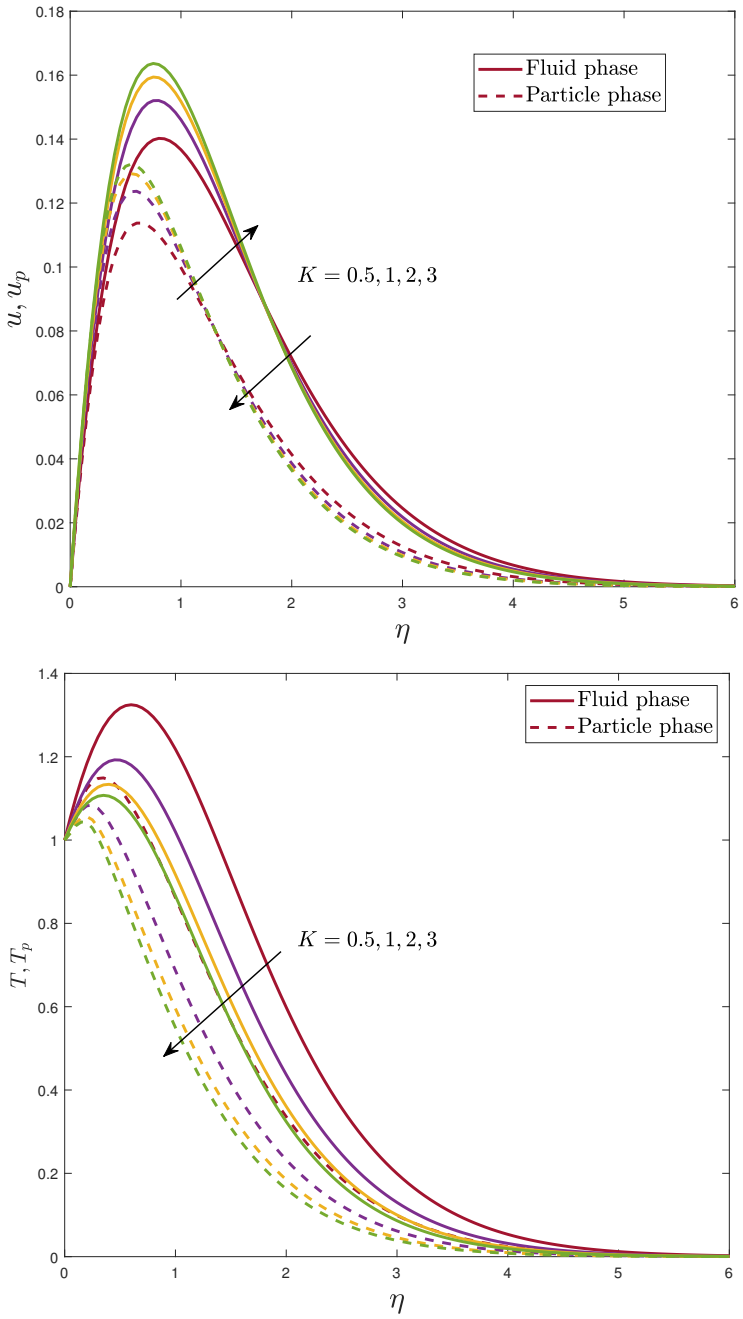

Figure 8: Impacts of porous permeability, K on velocity and temperature distribution

velocity. Meanwhile, heat absorption lowers buoyant forces, lowering fluid flow rates and decreasing the velocity field. This figure also shows that Q directly affects temperature distribution. Similar to the velocity profile, fluid temperature drops at $Q < 0$ and progressively rises at $Q > 0$. Figure 8 illustrates the effect of K on the velocity and temperature distribution. This graph indicates that both velocities are enhanced at $u : \eta \leq 1.75$ and $u_p : \eta \leq 1.3$, whereas they decline for $u : \eta > 1.75$ and $u_p : \eta > 1.3$ with rising K. In addition, when the value of K increases, the T and T_p decrease. This is because, the porous medium resistance to fluid motion increases as K increases, which improves the momentum development of the flow regime and,

as a consequence, increases both velocities while both temperatures drop steadily. However, beyond a certain point, higher permeability leads to increased interactions and disruptions, which in turn cause a decrease in velocity.

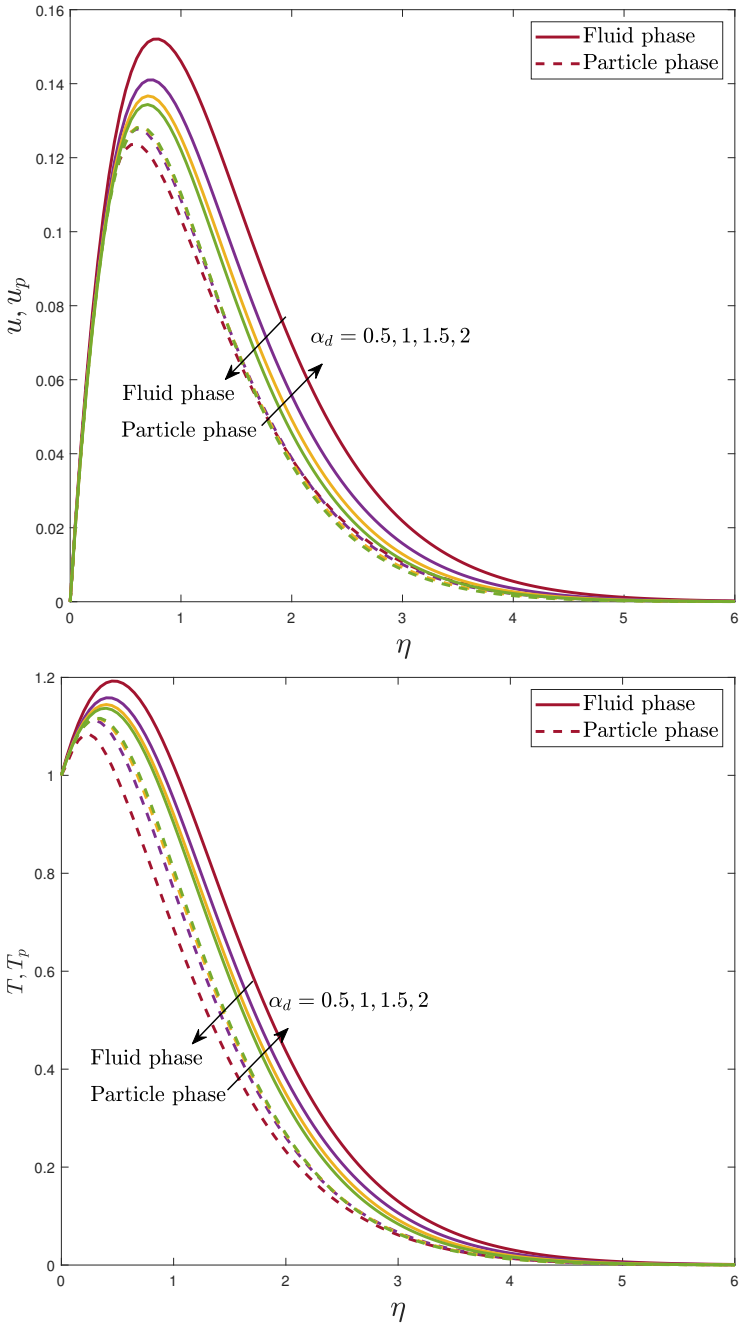

Figure 9: Impacts of fluid-particle interaction, α_d on velocity and temperature distribution

Figure 9 illustrates the effects of the parameter α_d on the distribution of velocity and temperature. A rise in α_d results in an amplification of u_p and T_p, while concurrently inducing a reduction in u and T. The particle phase generates a drag force that opposes the fluid phase, which is the cause of the observed outcome. This phenomenon, caused by momentum exchange between the fluid and particles, has been well-documented in the work of Rudinger (1980) and

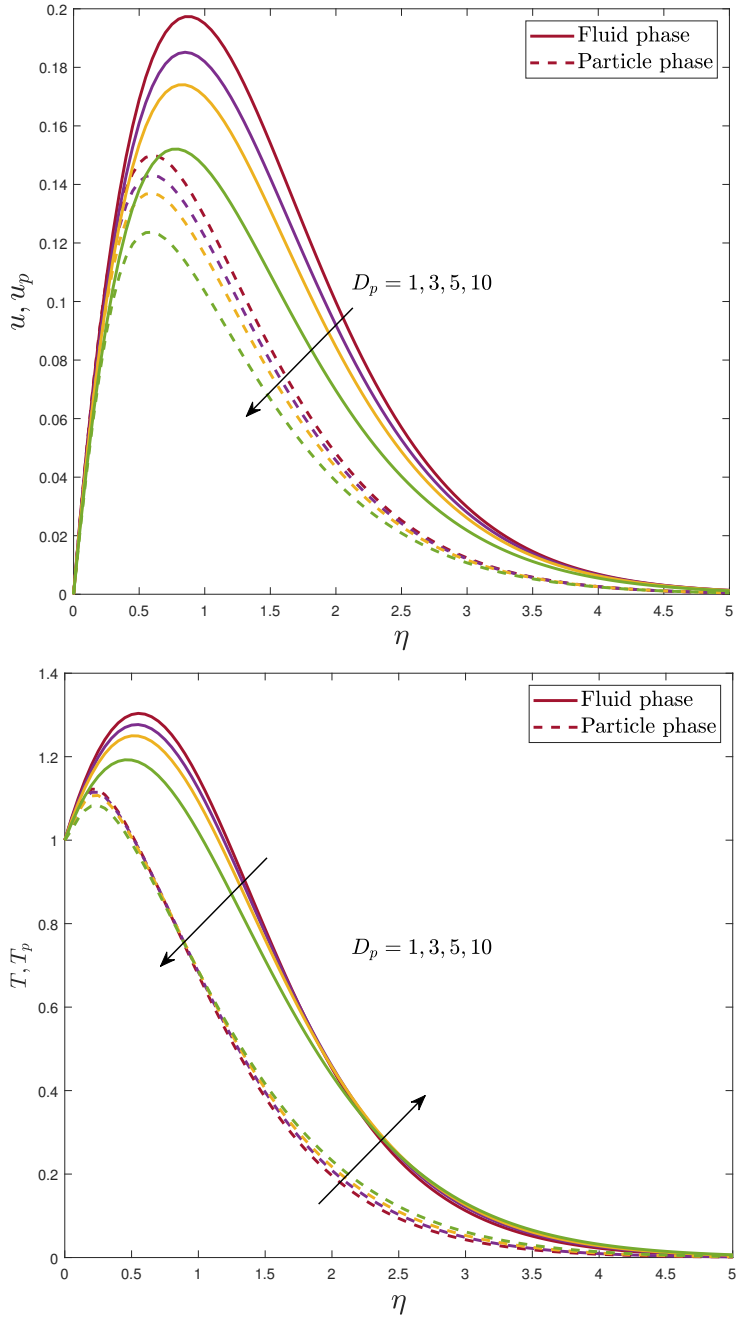

Figure 10: Impacts of mass concentration of particle phase parameter, D_p on velocity and temperature distribution

Saffman (1962). The distribution of fluid and particle velocity and temperature is affected by D_p, as seen in Figure 10. When D_p rises, both u and u_p are found to decrease, but both T and T_p reflect a dual nature. This graph indicates that both temperatures are decreasing at $T : \eta \leq 2.15$ and $T_p : \eta \leq 0.95$, whereas it increases for $T : \eta > 2.15$ and $T_p : \eta > 0.95$ with rising D_p.

The table that is shown in Table 2 provides an illustration of the influence that time, t, has on the Nusselt number, $-Nu_x/Gr_L{}^{\frac{1}{4}}$, and the wall shear stress, $\tau_x/Gr_L{}^{\frac{3}{4}}$. Over the course of

Table 2: Influence of t on $-Nu_x/Gr_L{}^{\frac{1}{4}}$ and $\tau_x/Gr_L{}^{\frac{3}{4}}$

t	Pr	D_p	γ	K	Rd	M	Q	α_d	-$Nu_\xi/Gr_L{}^{\frac{1}{4}}$	$\tau_x i/Gr_L{}^{\frac{3}{4}}$
1	7	10	0.1	2	1	2	0.5	0.5	-0.9666	0.1649
2.56									-0.2412	0.2313
3.94									0.1465	0.2798
6.36									0.6412	0.3554
8.81									0.8643	0.4002
10									0.9909	0.5178

Table 3: Variation of $-Nu_\xi/Gr_L{}^{\frac{1}{4}}$ and $\tau_\xi/Gr_L{}^{\frac{3}{4}}$ for different physical parameter

Pr	D_p	γ	K	Rd	M	Q	α_d	$-Nu_\xi/Gr_L{}^{\frac{1}{4}}$	$\tau_x i/Gr_L{}^{\frac{3}{4}}$
7	10	0.1	2	1	2	0.5	0.5	0.9909	0.5178
	3							0.9378	0.5018
	5							0.8843	0.4868
	10							0.7626	0.4541
			0.5					1.0030	0.4159
			1					0.6684	0.4769
			3					0.5587	0.4897
			2	0				1.3078	0.4610
				2				0.5608	0.4523
				4				0.3865	0.4513
				1	0			0.4875	0.5036
					1			0.6284	0.4769
					4			1.0030	0.4159
					2	-1		-1.9988	0.2181
						-0.5		-1.4412	0.2510
						0		0.6493	0.3128
						0.5	1	0.6930	0.4415
							1.5	0.6605	0.4358
							2	0.6421	0.4326

time, the values of local τ_ξ increase, whereas the values of local Nu_ξ are decrease. The table in Table 3 illustrates the variation of $-Nu_\xi/Gr_L{}^{\frac{1}{4}}$ and $\tau_\xi/Gr_L{}^{\frac{3}{4}}$ for different physical parameters. The observed trend indicates that the value of $-Nu_\xi/Gr_L{}^{\frac{1}{4}}$ increases with an increase in the quantities of M and Q, while it decreases with an increase in the quantities of D_p, K, Rd, and α_d. Augmenting M enhances the inhibition of heat transmission, thus resulting in an elevation of the local Nu_ξ. Moreover, increasing Q amplifies the internal heat sources, resulting in elevated temperature gradients and heightened local convective heat transport. Meanwhile, higher K facilitates fluid flow, reducing resistance and improving heat transfer. Besides, enhanced Rd influences the radiative heat exchange between surfaces. Increased D_p affects the particle distribution and interaction with the fluid. In addition, augmented α_d reduces the inhibiting effect of particles on heat transfer. Collectively, these effects lead to a decrease in local Nu_ξ. In addition, the value of $\tau_\xi/Gr_L{}^{\frac{3}{4}}$ increases with an elevation in the values of K and Q, whereas it decreases as the quantities of D_p, Rd, M, and α_d grow. Enhancing K promotes more efficient fluid flow and increasing Q results in increased internal heat effects, ultimately causing heightened local τ_ξ. Meanwhile, the intensified α_d decreases the resistance to fluid flow and the higher D_p affects the distribution and movement of particles. Besides, a stronger M alters fluid dynamics, and enhanced Rd alters the heat transfer characteristics. Together, these factors contribute to a reduction in the local τ_ξ. The surface temperature of the cone significantly influences the flow

and heat transfer characteristics observed in this study.

The elevated temperature of the cone surface establishes a strong temperature gradient, which drives natural convection and impacts both the thermal and velocity boundary layers. For instance, the results demonstrate that higher Pr lead to thinner thermal boundary layers and steeper temperature gradients, directly influenced by the cone's surface temperature. This gradient enhances the rate of heat transfer, as evidenced by the increased local Nu_ξ for higher Pr, highlighting the critical role of surface temperature in promoting effective thermal energy exchange. Additionally, the cone's surface temperature interacts with the fluid-particle system, altering the energy exchange dynamics between phases. The particle phase shows enhanced velocity near the surface due to the strong thermal gradient, while the fluid phase experiences a reduction in velocity, reflecting the influence of heat absorption and momentum exchange facilitated by the temperature difference. Molla *et al.* (2004) observed that surface geometry and fluid properties significantly impact these parameters, which aligns with the trends presented here.

4. Conclusion

The present study investigates the phenomenon of dusty flow in the presence of a magnetic field, thermal radiation, and heat generation/absorption over a vertical cone enclosed in porous media. Conical shapes are frequently employed in aircraft nose cones and fairings. The aerodynamics of these components are critical for reducing drag, optimising stability, and offering safe flight. Moreover, the study of dusty fluid flow around a cone could be utilized to test aircraft models in wind tunnels. The findings of this research are summarized below:

- As the Prandtl number increases in both the fluid and dust phases, the velocity and temperature profiles of the fluid and dust phase decrease. Moreover, the values required to achieve a steady state increase for the velocity profile while decreasing for the temperature profile.
- Elevating the thermal radiation and heat generation/absorption parameters results in an augmentation of the velocity profile for the fluid and dust phases while conversely affecting the mass concentration of the particle phase parameter.
- An increase in the velocity profile leads to the manifestation of a dual nature in both the magnetic and porosity parameters.
- As the temperature distribution expands, it is found that while the porosity parameter shows the opposite tendency, the magnetic and heat generation/absorption parameters increase.
- As the temperature profile rises, a duality is observed in the thermal radiation parameter and the mass concentration of the particle phase parameter.
- The fluid-particle interaction parameter enhances the velocity and temperature of the dust phase, while reducing the velocity and temperature of the fluid phase.
- This paper focused on a specific geometry known as the vertical cone. This problem can potentially be extended using different geometries.
- This study focused on the dusty fluid which is a Newtonian fluid. Dusty fluid also can be studied with non-Newtonian fluids.

Acknowledgments

The authors would like to acknowledge the Ministry of Higher Education Malaysia, UTM Zamalah and Research Management Centre-UTM, for financial support under the UTM Fundamental Research (UTMFR) Grant Q.J130000.3854.23H22.

Appendix

Table 4: List of symbols with descriptions and SI units

Symbol	Description	SI Unit
ρ, ρ_p	Density	kg/m^3
β_T	Volumetric thermal expansion coefficient	1/K
τ_m	Momentum relaxation time	s
k_0	Permeability constant	m^2
τ_T	Thermal relaxation time	s
k_e	Absorption coefficient	m^{-1}
B	Magnetic field	T
M	Magnetic field parameter	Dimensionless
σ	Electrical conductivity	S/m
K	Porous permeability parameter	Dimensionless
k	Thermal conductivity	W/(m·K)
D_p	Particle phase mass concentration parameter	Dimensionless
σ_s	Stefan–Boltzmann constant	W/(m^2·K^4)
Rd	Thermal radiation parameter	Dimensionless
q_r	Radiative heat flux	W/m^2
α_d	Fluid-particle interaction parameter	Dimensionless
Pr	Prandtl number	Dimensionless
Nu_ξ	Nusselt number	Dimensionless
Q_0, Q	Heat generation/absorption parameter	W/m^3
g	Gravitational acceleration	m/s^2
τ_ξ	Wall shear stress	Pa
γ	Mixture specific heat ratio	Dimensionless
α	Cone half angle	Radians
$\boldsymbol{\nabla}$	Gradient operator $\left(\frac{\partial}{\partial x}, \frac{\partial}{\partial y}\right)$	1/m
$\mathbf{V}, \mathbf{V}_p$	Velocity components $\big((u, v), (u_p, v_p)\big)$	m/s
μ	Dynamic viscosity	Pa·s
C_p	Specific heat at constant pressure	J/(kg·K)
Gr_L	Grashof number	Dimensionless
C_s	Specific heat for the particle phase	J/(kg·K)
Subscripts		
p	Particle phase	
$*$	Non-dimensional	

References

Adak M. 2018. Comparison of explicit and implicit finite difference schemes on diffusion equation. *Proceedings of the International Conference on Applied and Computational Mathematics*, pp. 227–238.

Ahmad S., Farooq M., Anjum A. & Mir N.A. 2019. Squeezing flow of convectively heated fluid in porous medium with binary chemical reaction and activation energy. *Advances in Mechanical Engineering* **11**(10): 1687814019883774.

Anand V.W.J., Ganesh S., Ismail A.M. & Kirubhashankar C.K. 2015. Unsteady MHD dusty fluid flow of an exponentially stretching sheet with heat source through porous medium. *Applied Mathematical Sciences* **9**(42): 2083–2090.

Attia H.A. & Ewis K.M. 2019. Magnetohydrodynamic flow of continuous dusty particles and non-Newtonian Darcy fluids between parallel plates. *Advances in Mechanical Engineering* **11**(6): 1687814019857349.

Attia H.A., Ewis K.M. & Abd Elmaksoud I.H. 2012. Numerical study of unsteady circular pipe flow of a dusty fluid through a porous medium. *Proceedings of the International Conference on Mathematics and Engineering Physics*, pp. 1–7.

Bear J. 2013. *Dynamics of Fluids in Porous Media*. Mineola, NY: Courier Corporation.

Bibi M., Zeeshan A. & Malik M.Y. 2022. Numerical analysis of unsteady momentum and heat flow of dusty tangent hyperbolic fluid in three dimensions. *Scientific Reports* **12**(1): 16079.

Blottner F.G. 1970. Finite difference methods of solution of the boundary-layer equations. *AIAA Journal* **8**(2): 193–205.

Chamkha A.J., Rashad A.M. & Al-Mudhaf H.F. 2012. Heat and mass transfer from truncated cones with variable wall temperature and concentration in the presence of chemical reaction effects. *International Journal of Numerical Methods for Heat & Fluid Flow* **22**(3): 357–376.

Chand K. 2018. Hydromagnetic oscillatory flow and heat transfer in dusty viscoelastic fluid through porous medium in an inclined channel in the presence of thermal radiation and heat sink. *International Journal of Mathematics Trends and Technology* **53**(5): 397–408.

Fathy M. & Sayed E.A. 2022. Maxwell dusty fluid flow past a variable thickness porous stretching surface. *Mathematical Modelling and Engineering Problems* .

Hamid R.A., Nazar R. & Pop I. 2018. Numerical solutions for unsteady boundary layer flow of a dusty fluid past a permeable stretching/shrinking surface with particulate viscous effect. *International Journal of Numerical Methods for Heat & Fluid Flow* **28**(6): 1374–1391.

Hanif H., Khan I. & Shafie S. 2020. Heat transfer exaggeration and entropy analysis in magneto-hybrid nanofluid flow over a vertical cone: A numerical study. *Journal of Thermal Analysis and Calorimetry* **141**(5): 2001–2017.

Hasan M. & Mujumdar A.S. 1984. Coupled heat and mass transfer in natural convection under flux condition along a vertical cone. *International Communications in Heat and Mass Transfer* **11**(2): 157–172.

Hering R. & Grosh R. 1962. Laminar free convection from a non-isothermal cone. *International Journal of Heat and Mass Transfer* **5**(11): 1059–1068.

Immanuel Y., Pullepu B. & Maheshwaran T. 2019. Group method study of steady laminar natural convection flow past an isothermal vertical cone. *AIP Conference Proceedings* **2112**(1): 020064.

Isa S.M., Ali A. & Shafie S. 2016. Magnetohydrodynamic flow of dusty fluid past a vertical stretching sheet with Hall effect. *AIP Conference Proceedings* **1750**(1): 020005.

Jagannadham N., Rath B.K. & Dash D.K. 2022. Numerical solution of fluid and particle phase on velocity of heat with effect of magnetic field in incompressible dusty fluid. *Dogo Rangsang Research Journal* **12**(10): 120–127.

Kays W.M. & Crawford M.E. 1980. *Convective Heat and Mass Transfer*. 2nd Ed. New York: McGraw-Hill.

Khan D., Asogwa K.K., Kumam P., Watthayu W., Kumam W. & Almusawa M.Y. 2023. Inclined relative magnetic field analysis of Brinkman-type dusty fluid through fluctuating upright parallel plates. *Heliyon* **9**(4): e14770.

Kliegel J.R. & Nickerson G.R. 1962. Flow of gas-particle mixtures in axially symmetric nozzles. In Penner S.S. & Williams F.A. (eds.). *Detonation and Two-Phase Flow*: 173-194. New York: Academic Press.

Luskin M., Rannacher R. & Wendland W. 1982. On the smoothing property of the Crank-Nicolson scheme. *Applicable Analysis* **14**(2): 117–135.

Madhura K.R. & Uma M.S. 2016. Conducting dusty fluid flow through a constriction in a porous medium. *International Journal of Applied Mathematics Research* **5**(1): 29–38.

Magyari E. & Pantokratoras A. 2011. Note on the effect of thermal radiation in the linearized Rosseland approximation on the heat transfer characteristics of various boundary layer flows. *International Communications in Heat and Mass Transfer* **38**(5): 554–556.

Mahabaleshwar U.S., Maranna T., Pérez L.M., Bognár G.V. & Oztop H.F. 2023. An impact of radiation on laminar flow of dusty ternary nanofluid over porous stretching/shrinking sheet with mass transpiration. *Results in Engineering* **18**: 101227.

Manjunatha S.S., Gireesha B.J., Eshwarappa K.M. & Bagewadi C.S. 2013. Similarity solutions for boundary layer flow of a dusty fluid through a porous medium over a stretching surface with internal heat generation/absorption. *Journal of Porous Media* **16**(6): 501–514.

Mohiddin S.G., Beg O.A. & Varma S.V.K. 2012. Unsteady free convective heat and mass transfer past a vertical cone in non-darcian porous media. *International Journal of Computer Applications* **56**(7): 17–25.

Molla M.M., Hossain M.A. & Yao L.S. 2004. Natural convection flow along a vertical wavy surface with uniform surface temperature in presence of heat generation/absorption. *International Journal of Thermal Sciences* **43**(2):

157–163.
Nabwey H.A. & Mahdy A. 2021. Numerical approach of micropolar dust-particles natural convection fluid flow due to a permeable cone with nonlinear temperature. *Alexandria Engineering Journal* **60**(1): 1739–1749.
Palani G. & Lalith Kumar E.J. 2021. Dusty gas flow over a semi-infinite vertical cone. *JP Journal of Heat and Mass Transfer* **22**(2): 201–216.
Pullepu B., Chamkha A.J. & Pop I. 2012. Unsteady laminar free convection flow past a non-isothermal vertical cone in the presence of a magnetic field. *Chemical Engineering Communications* **199**(3): 354–367.
Pullepu B., Ekambavanan K. & Chamkha A.J. 2007. Unsteady laminar natural convection from a non-isothermal vertical cone. *Nonlinear Analysis: Modelling and Control* **12**(4): 525–540.
Rafiq M., Siddiqa S., Begum N., Al-Mdallal Q., Hossain M.A. & Gorla R.S.R. 2021. Non-linear radiation effect on dusty fluid flow near a rotating blunt-nosed body. *Proceedings of the Institution of Mechanical Engineers, Part E: Journal of Process Mechanical Engineering* **235**(6): 1775–1783.
Rahman M., Waheed H., Turkyilmazoglu M. & Siddiqui M.S. 2024. Darcy-Brinkman porous medium for dusty fluid flow with steady boundary layer flow in the presence of slip effect. *International Journal of Modern Physics B* **38**(11): 2450152.
Reddimalla N., Ramana Murthy J.V., Radha Krishna Murthy V. & Jangili S. 2022. Effect of magnetic field on unsteady flow of dusty fluid due to constant pressure gradient through a circular cylinder: An analytical treatment. *Proceedings of the 5th International Conference on Applications of Fluid Dynamics (ICAFD)*, pp. 195–202.
Rudinger G. 1980. *Fundamentals of Gas-Particle Flow*. Amsterdam: Elsevier Scientific Publishing Company.
Saffman P.G. 1962. On the stability of laminar flow of a dusty gas. *Journal of Fluid Mechanics* **13**(1): 120–128.
Sambath P. 2017. A study on unsteady natural convective flow past a vertical cone with heat and mass transfer effects. PhD Thesis. SRM Institute of Science and Technology.
Sandeep N., Sulochana C. & Kumar B.R. 2016. Unsteady MHD radiative flow and heat transfer of a dusty nanofluid over an exponentially stretching surface. *Engineering Science and Technology, an International Journal* **19**(1): 227–240.
Saxena P. & Agarwal M. 2014. Unsteady flow of a dusty fluid between two parallel plates bounded above by porous medium. *International Journal of Engineering, Science and Technology* **6**(1): 27–33.
Siddiqa S., Begum N., Hossain A.M. & Gorla R.S.R. 2018a. Numerical solution of contaminated oil along a vertical wavy frustum of a cone. *Thermal Science* **22**(6 Part B): 2933–2942.
Siddiqa S., Begum N., Hossain M.A., Mustafa N. & Gorla R.S.R. 2017. Two-phase dusty fluid flow along a cone with variable properties. *Heat and Mass Transfer* **53**(5): 1517–1525.
Siddiqa S., Begum N., Ouazzi A., Hossain M.A. & Gorla R.S.R. 2018b. Heat transfer analysis of Casson dusty fluid flow along a vertical wavy cone with radiating surface. *International Journal of Heat and Mass Transfer* **127**: 589–596.
Sivaraj R. & Kumar B.R. 2013. Viscoelastic fluid flow over a moving vertical cone and flat plate with variable electric conductivity. *International Journal of Heat and Mass Transfer* **61**: 119–128.
Sproull W.T. 1961. Viscosity of dusty gases. *Nature* **190**(4780): 976–978.
Sun G. & Trueman C.W. 2006. Efficient implementations of the Crank-Nicolson scheme for the finite-difference time-domain method. *IEEE Transactions on Microwave Theory and Techniques* **54**(5): 2275–2284.
Thandapani E., Ragavan A.R. & Palani G. 2012. Finite-difference solution of unsteady natural convection flow past a nonisothermal vertical cone under the influence of a magnetic field and thermal radiation. *Journal of Applied Mechanics and Technical Physics* **53**(3): 408–421.
Vidhya M., Niranjana N. & Govindarajan A. 2017. Free convective and oscillatory flow of a dusty fluid through a porous medium. *International Journal of Pure and Applied Mathematics* **114**(3): 445–456.

Department of Mathematical Sciences
Faculty of Science
Universiti Teknologi Malaysia
81310 Johor Bahru
Johor, MALAYSIA
*E-mail: shajar263@live.utm.my, jiann@utm.my, sharidan@utm.my**

Department of Mathematics
Sardar Bahadur Khan Women's University
87300 Balochistan
Quetta, PAKISTAN
E-mail: hanifahanif@outlook.com

Received: 27 January 2025
Accepted: 30 May 2025

*Corresponding author